

Quantum annealing of Cayley-tree Ising spins

Yunheung Song,^{*} Minhyuk Kim, Hansub Hwang, Woojun Lee,[†] and Jaewook Ahn[‡]

Department of Physics, Korea Advanced Institution of Science and Technology, Daejeon 34141, Republic of Korea

(Dated: February 22, 2021)

Significant efforts are being directed towards developing a quantum annealer capable of solving combinatorial optimization problems. The challenges are Hamiltonian programming in terms of high dimensional qubit connectivity and large-scale implementations. Here we report quantum annealing demonstration of Ising Hamiltonians programmed with up to $N = 22$ spins mapped on various Cayley-tree graphs. Experiments are performed with a Rydberg-atom quantum simulator, in which rubidium single atoms are arranged in three dimensional space in such a way that their Rydberg atoms and blockaded strong couplings respectively represent the vertices and edges of each graph. Three different Cayley-tree graphs of $Z = 3$ neighbors and of up to $S = 4$ shells are constructed, and their ground-state phases and Néel's order formations are probed. The anti-ferromagnetic phase in regular Cayley trees and frustrated competing ground-states in a dual-center Cayley tree are directly observed, demonstrating the possibilities of high-dimensional qubit connections in quantum simulators.

I. INTRODUCTION

In recent years, quantum annealers have received significant attention because of their potentials in solving complex computational problems which are often intractable with non-quantum computational methods [1–4]. Quantum annealing is a procedure of making Hamiltonian $H(t)$ of a quantum many-body system adiabatically evolve from \hat{H}_i to \hat{H}_f ,

$$\hat{H}(t) = \hat{H}_i - \frac{t}{t_f}(\hat{H}_i - \hat{H}_f), \quad (1)$$

so that the quantum state $|\Psi(t)\rangle$ initially prepared in the ground state of the former reaches the ground state of the later. Quantum annealers are considered with superconducting qubits [5–8] and trapped-ion qubits [9–12], aiming for various combinatorial optimization problems such as quantum simulations [13], classifications [14], planning [15], etc. While many efforts in quantum annealing are being focused on large-scale implementations [16–20] towards quantum speedup [21–24], here we explore the possibility of high-dimensional qubit connectivities. There are theoretical proposals emphasizing and thus utilizing qubit connectivities for NP-hard optimization problems: for examples, Lechner-Hauke-Zoller scheme [25, 26] proposed a quantum annealing architecture for all-to-all connectivities using local interactions; and quantum optimization protocols are considered, e.g., for maximum independent set problems utilizing the nature of long-range couplings especially in Rydberg-atom quantum simulators [27]. In the context relevant to the present work, Rydberg-atom quantum simulators [28, 29]

draw attention, because of their high tunability in qubit connectivities [30–34] as well as many-body controllability in adiabatic processes [35–39].

In this work, we consider, as a prototypical fractal structures, Cayley tree graphs of neutral atom arrangements, in which atoms and strongly interacting atom pairs respectively represent vertices and edges of the graphs (see Fig. 1). Cayley trees are homogeneous and isotropic tree graphs of a fixed number of edges and no loop [40, 41]. Their infinite version is Bethe lattice widely used in various physics areas as a fundamental theoretical platform, often providing exactly solvable models in classical and quantum problems [42]. In experiments to be described below, we construct atomic Cayley graphs of coordination number $Z = 3$ and shell number up to $S = 4$, as in Fig. 1(a), and use a Rydberg-atom quantum simulator to directly probe their Ising-Hamiltonian phases.

II. CAYLEY-TREE ATOM ARRANGEMENTS IN THREE-DIMENSIONAL SPACE

Neutral atoms (rubidium, ^{87}Rb) are arranged in three-dimensional (3D) space with optical tweezers (far-off resonant optical dipole traps) [34, 43] (see Sec. VI for technical details). Three different Cayley-tree graphs are constructed. The first one is the three-shell ($S = 3$) Cayley tree, which can be denoted by $G_{10} = (0s)(1s)^3(2s)^6$, having one in the first (center) shell, three in the second shell, and six in the third shell, as in Fig. 1(b). The second one is the four-shell ($S = 4$) Cayley tree, $G_{22} = (0s)(1s)^3(2s)^6(3s)^{12}$, having ten atoms in G_{10} and twelve in the fourth shell, as in Fig. 1(c). And the last one is $G_{14} = (0s)^2(1s)^4(2s)^8$, a dual-center Cayley tree, having two first-shell atoms, four second-shell atoms, and eight third-shell atoms, as in Fig. 1(d).

In our atom arrangements, each atom represents a vertex of a Cayley-tree graph and each pair of strongly-interacting atoms an edge. Non-connected atoms are

^{*}Present address: Department of Physics, University of Wisconsin-Madison, 1150 University Avenue, Madison, Wisconsin 53706, USA

[†]Present address: Department of Computer Science and Engineering, Seoul National University, Seoul 08826, Republic of Korea

[‡]jwahn@kaist.ac.kr

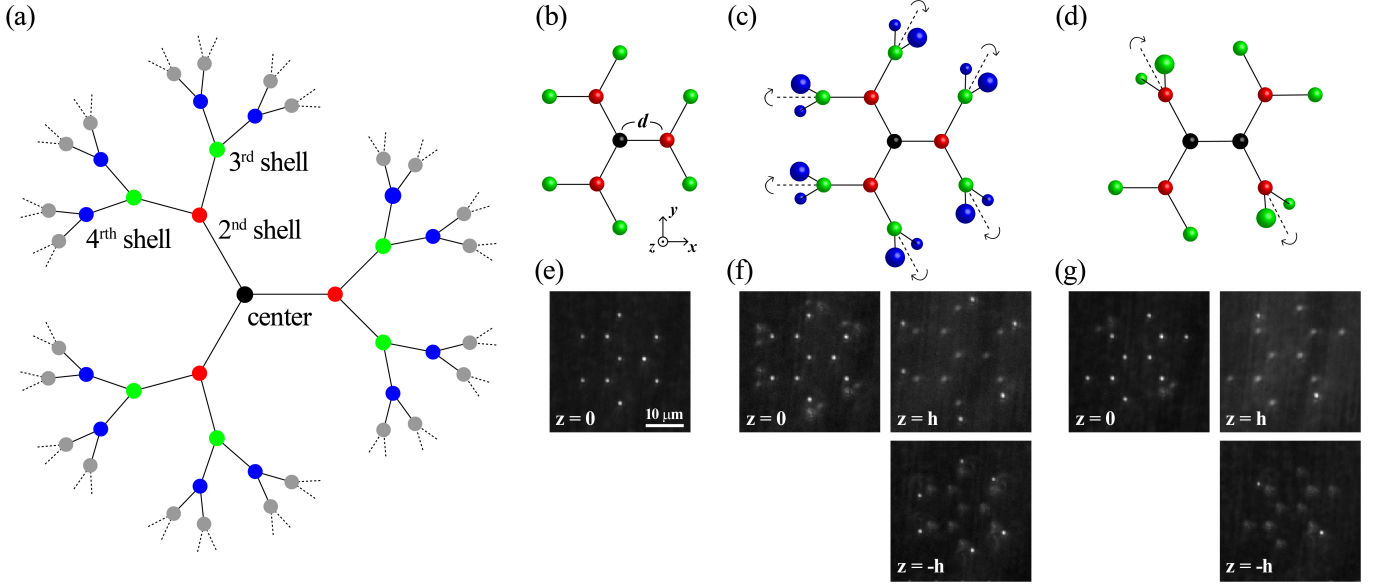


FIG. 1: (a) A generic Cayley-tree graph of coordination number $Z = 3$, with vertices and edges representing atoms and Rydberg-blockaded atom pairs, respectively. (b) A three-shell Cayley tree (G_{10}) of 10 atoms of inter-atom distance d . (c) A four-shell Cayley tree (G_{22}) constructed in three planes at $z = 0, \pm h$ ($h = d/1.2$), where the last-shell branches are rotated by 72° to avoid unwanted couplings. (d) A dual-center Cayley tree (G_{14}) of 14 atoms. (e, f, g) Plane-by-plane fluorescence images of the corresponding atom arrangements.

supposed to interact with each other much weakly than connected atoms. The Hamiltonian of these atoms being coherently and simultaneously excited to a Rydberg energy state is given (in unit of $\hbar = 1$) by

$$\hat{H} = \frac{1}{2} \sum_{j=1}^N \left\{ \Omega \hat{\sigma}_x^{(j)} - \Delta \hat{\sigma}_z^{(j)} \right\} + \sum_{j < k} U_{jk} \hat{n}^{(j)} \hat{n}^{(k)}, \quad (2)$$

where N is the number of atoms, Ω is the Rabi frequency, Δ is the detuning, and $U_{jk} = C_6/|\vec{r}_j - \vec{r}_k|^6$ is the pairwise atom interaction in the van der Waals interaction regime [37, 38]. Pauli operators $\hat{\sigma}_{x,z}$ are defined for a pseudo spin 1/2 system composed of the ground state $|\downarrow\rangle = |5S_{1/2}, F=2, m_f=2\rangle$ and Rydberg state $|\uparrow\rangle = |71S_{1/2}, F'=3, m_{F'}=3\rangle$ of each atom, and $\hat{n} = (1 + \hat{\sigma}_z)/2$. For the strong and weak interactions of connected and nonconnected atom pairs, respectively, we set the distances of connected atoms the same and within the Rydberg-blockade radius, i.e., $|\vec{r}_j - \vec{r}_k| = d < r_b \equiv (C_6/\hbar\Omega)^{1/6} = 9.8 \mu\text{m}$, for $(j, k) \in E$ (the edge set of a graph G), and the distances of all others are $|\vec{r}_j - \vec{r}_k| > r_b$.

The two-dimensional (2D) arrangement of G_{10} is made with $d < r_b < \sqrt{3}d$ to satisfy the above condition, in which, as shown in Fig. 1(e), the last-shell atoms of different branches are separated more than $\sqrt{3}d$, having at most 1/27 times smaller interactions than $U \equiv C_6/d^6$ of the connected atom pairs. However, G_{22} and G_{14} cannot be planar, because in 2D arrangements, atoms of different outermost branches are too close, requiring nonplanar, three-dimensional (3D) arrangements. As shown in Fig. 1(c), we rotate the last-shell branches of G_{22} by an

angle of $2\pi/5$ about the axes along the previous branches, so that all the last-shell atoms are well separated (more than $\sqrt{3}d$) from each other. In G_{14} , some last-shell branches are rotated similarly, as shown in Fig. 1(d). As-constructed atom arrangements are shown in Figs. 1(e-g) respectively for G_{10} , G_{22} , and G_{14} .

III. PHASE DIAGRAMS OF CAYLEY-TREE ISING SPINS

With atoms arranged on one of the above Cayley-tree graphs, we perform quantum annealing to find the ground state of a target Hamiltonian. The atoms are initially prepared in $|\downarrow\downarrow\cdots\downarrow\rangle$ (the paramagnetic down spins in Phase I) under the Hamiltonian conditions of $\Delta \gg U$ and $\Omega = 0$ in \hat{H} . The target (final) Hamiltonian is

$$\hat{H}_G(U, \Delta_f) = U \sum_{(j,k) \in E} \hat{n}^{(j)} \hat{n}^{(k)} - \frac{\Delta_f}{2} \sum_{j=1}^N \hat{\sigma}_z^{(j)} \quad (3)$$

where E is the edge set of $G \in \{G_{10}, G_{22}, G_{14}\}$, Δ_f is the final detuning, and no couplings are assumed for un-edged atom pairs. We note that \hat{H}_G is an Ising spin-glass Hamiltonian, given by

$$\hat{H}_G = J \sum_{(j,k) \in E} \hat{\sigma}_z^{(j)} \hat{\sigma}_z^{(k)} + h_z^C \sum_{j \in C} \hat{\sigma}_z^{(j)} + h_z^V \sum_{j \in V} \hat{\sigma}_z^{(j)}, \quad (4)$$

where $J = U/4$ is the coupling, $h_z^C = 3U/4 - \Delta_f/2$ and $h_z^V = U/4 - \Delta_f/2$ are the local fields, and C and V denote the vertices in the core (inner shells) and valence

(outermost) shell, respectively, of a Cayley-tree graph $G(E, C + V)$. In general, as the ground-states of an Ising Hamiltonian depend on the specific atom arrangement of G , finding such arrangement-specific ground-states of an arbitrary Ising-spin graph is an NP-complete problem [44].

However, Cayley-tree graphs allow heuristic understanding of their phase diagrams as follows: Cayley trees have more atoms on the valence shell than on the rest (the inner shells) of a tree. Therefore, with Hamiltonian \hat{H}_G in Eq. (3) (of positive coupling, $U > 0$, in our consideration), the valence spins are all aligned either up or down depending upon $\Delta_f > 0$ or $\Delta_f < 0$, respectively, resulting in the $\Delta_f = 0$ phase boundary. For $\Delta_f < 0$, inner-shell spins, adjacent to the valence spins, also favor down spins, as their couplings, $U\hat{n}^{(j)}\hat{n}^{(k)}$, to adjacent outer-shell down spins are zero, which sequentially results in all down spins (so paramagnetic down spins, Phase I). For $\Delta_f > 0$, the single-spin flipping energy (Δ_f) competes with adjacent anti-ferromagnetic couplings. For $\Delta_f > 3U$, the former is always higher than the latter (of max $3U$), so all spins are up (paramagnetic up spins, Phase II). In between, $0 < \Delta_f < 3U$, the anti-ferromagnetic coupling is stronger, thus favoring the anti-ferromagnetic phase (Phase III) of shell-by-shell alternating spins. The resulting \hat{H}_G phase diagram is shown for G_{10} in Fig. 2(a), in which the anti-ferromagnetic phase (Phase III) has up spins on the first and third shells and down spins on the second. The phase diagram for G_{22} differs from G_{10} only in Phase III, where the odd-number shells are down spins and the even-number shells are up spins. In short, the phase diagram of \hat{H}_G (of positive U) for regular Cayley-graphs (G_{10} and G_{22} in our consideration) has the para-antiferro phase boundaries determined by $\Delta_f = 3U$ and $\Delta_f = 0$, so the anti-ferromagnetic ordering is expected in the region $0 < \Delta_f < 3U$ (Phase III), as in Fig. 2(a).

The phase diagram for G_{14} , the dual-center Cayley tree, is a little more complex than regular Cayley trees, because of the frustrations of the center spins. Exact diagonalization of $\hat{H}_{G_{14}}$ finds the phase diagram as shown in Fig. 3(b), in which the paramagnetic phases (Phases I and II) are the same as G_{10} , but Phase III is split to Phases IV and V, of respective center-spin configurations of $|\uparrow\uparrow\rangle$ and $(|\uparrow\downarrow + \downarrow\uparrow\rangle)/\sqrt{2}$. The new phase boundary is $U = \Delta_f$, along which the single-spin flipping cost equals the additional frustration cost of the center spins. It is noted that, in Phase V, other energy-degenerate ground states, with respective center-spin configurations of $|\uparrow\downarrow\rangle$, $|\downarrow\uparrow\rangle$, and $(|\uparrow\downarrow - \downarrow\uparrow\rangle)/\sqrt{2}$, are all dark states for a quantum annealing performed to the given initial state, due to the symmetry of \hat{H} in Eq. (2).

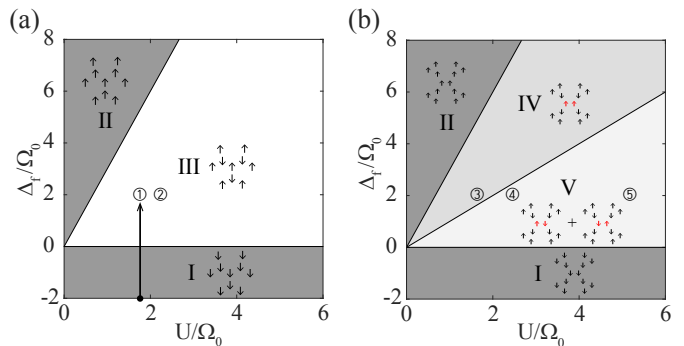


FIG. 2: Phase diagrams of Cayley-tree Ising Hamiltonians (a) $\hat{H}_{G_{10}}$ and $\hat{H}_{G_{22}}$ and (b) $\hat{H}_{G_{14}}$, in which ground-state spin configurations are paramagnetic down spins (Phase I), paramagnetic up spins (Phase II), antiferromagnetic phase (Phase III), and antiferro-like phases with center-spins $|\uparrow\uparrow\rangle$ (Phase IV) and $(|\uparrow\downarrow + \downarrow\uparrow\rangle)/\sqrt{2}$ (Phase V). Circled numbers indicate the Hamiltonian parameters of the experimental data in Figs. 3 and 4: ① ($U/\Omega_0, \Delta_f/\Omega_0$)=(1.82, 2) in Phase III of G_{10} , ② (2.25, 2) in Phase III of G_{22} , ③ (1.67, 2) in Phase IV of G_{14} , ④ (2.70, 2) and ⑤ (5.41, 2) in Phase V of G_{14} . $\Omega_0 = 1.1$ (2 π)MHz in all experiments.

IV. EXPERIMENTAL VERIFICATION OF CAYLEY-TREE ISING PHASES

Experiments are performed to verify the antiferro-like ground states (the Phases III, IV, and V) of Cayley-tree Ising spins (see Sec. VI for technical details). Quantum annealing is preceded with three stages of time evolution, along a vertical control path from Phase I to either Phase III, IV or V in Fig. 2. In the first stage ($0 < t < 0.1t_f$), Rabi frequency is adiabatically turned on from $\Omega_i = 0$ to $\Omega_0 = 1.1(2\pi)$ MHz, while detuning is maintained at $\Delta = -2\Omega_0$ for the paramagnetic down-spin ordering ($|\hbar_z^{C,V}| \gg J$) of Phase I. In the second stage ($0.1 < t/t_f < 0.9$), the detuning is swept from $-2\Omega_0$ to $2\Omega_0$, while the Rabi frequency is maintained at Ω_0 . In the final stage ($0.9 < t/t_f < 1$), the detuning is maintained at $\Delta_f = 2\Omega_0$ (for anti-ferromagnetic ordering, $0 < \Delta_f < 3U$) and the Rabi frequency is adiabatically turned off from Ω_0 to $\Omega_f = 0$. The total operation time $t_f = (2\pi)3.2/\Omega_0 = 2.9 \mu\text{s}$ is chosen long enough to identify the max-population states and short compared to the coherence time of $10 \mu\text{s}$ [43]. After the time evolution, the resulting spin configuration is detected and the procedure is repeated until the probability distribution of all spin configurations is obtained. The final Hamiltonians $\hat{H}_G(U, \Delta_f = 2\Omega_0)$ are chosen at various phases in Fig. 2: ① and ② for Phase III of G_{10} and G_{22} , respectively; ③ for Phase IV of G_{14} ; and ④ and ⑤ for Phase V of G_{14} .

Measured probability distributions are shown in Figs. 3(a-c), which plot the probability distributions, respectively measured at ①, ②, and ④, for all spin configurations of the Cayley-tree Ising spins. Spin configura-

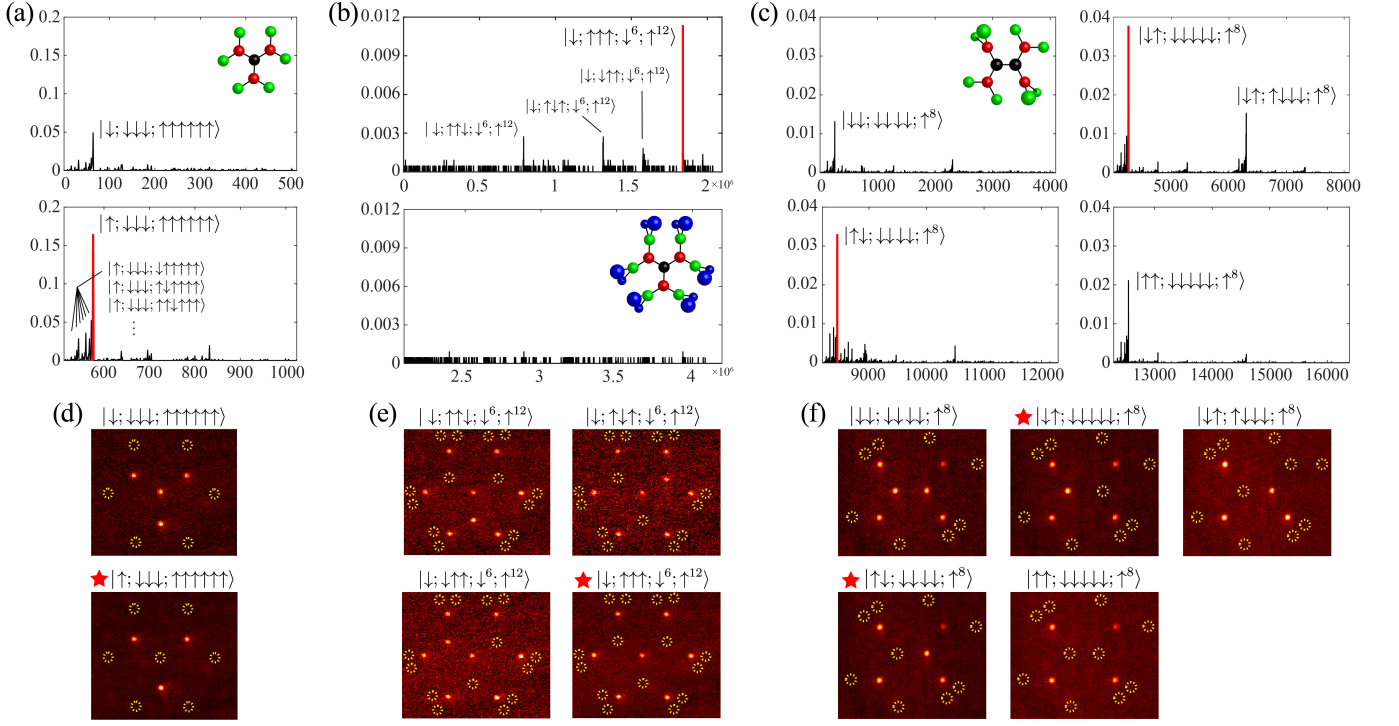


FIG. 3: Probability distribution of all spin configurations in enumerated bare-spin basis: (a) G_{10} Cayley-tree atoms measured at ① in Phase III and accumulated over 672 events. (b) G_{22} at ② in Phase III (2208 events). (c) G_{14} at ④ in Phase V (5113 events). Max populations are ground states (highlighted in red) and smaller peaks are identified near-ground excited states. (d,e,f) Fluorescence images of ground-state ($|\downarrow\rangle$) atoms in characteristic spin configurations.

tions are represented in the bare-atom basis with binary enumeration of $|\downarrow\rangle = |0\rangle$ and $|\uparrow\rangle = |1\rangle$ [45]. After the quantum annealing, the wavefunction of the atoms is expectedly driven near the ground state of $\hat{H}_G(U, \Delta_f)$, so the corresponding spin configuration is measured with a high probability. In Fig. 3(a), Phase III of G_{10} is probed at ①. The observed max-population state is $|\uparrow; \downarrow\downarrow; \uparrow\uparrow\uparrow\uparrow\rangle = |2^9 + 2^5 + 2^4 + 2^3 + 2^2 + 2^1 + 2^0\rangle = |575\rangle$, which is the anti-ferromagnetic phase of shell-by-shell alternating spins, agreeing with the expected ground state of $\hat{H}_{G_{10}}$ in Phase III. Likewise, in Figs. 3(b), Phase III of G_{22} is probed at ② and the observed $|\downarrow; \uparrow^3; \downarrow^6; \uparrow^{12}\rangle = |1839103\rangle$ agrees with the ground-state of $\hat{H}_{G_{22}}$ in Phase III. In Fig. 3(c), which shows the measurement of G_{14} at ④ in Phase V, high populations are observed for $|\downarrow\uparrow; \downarrow^4; \uparrow^8\rangle = |4351\rangle$ and $|\uparrow\uparrow; \downarrow^4; \uparrow^8\rangle = |8447\rangle$, agreeing with the ground superposition state (of center spins in $(|\uparrow\downarrow\rangle + |\downarrow\uparrow\rangle)/\sqrt{2}$) in Phase V of $\hat{H}_{G_{14}}$. Atom images (the fluorescence of ground-state atoms) of characteristic spin configurations are shown in Figs. 3(d,e,f), including the max-population states (of star marks).

Phase IV of G_{14} is also probed acrossing the IV-V phase boundary, with three different Cayley trees of respective edge lengths $d/r_b = 0.76, 0.86,$ and 0.92 , which correspond to ⑤, ④, and ③ in the phase diagram. In Fig. 4, the probabilities of three high-population states,

of respective center-spin configurations $|\uparrow\uparrow\rangle, |\downarrow\downarrow\rangle,$ and $(|\uparrow\downarrow\rangle + |\downarrow\uparrow\rangle)/\sqrt{2}$, are plotted. The max-populated state changes from $|\uparrow\uparrow\rangle$ ($d < d_c = 0.89r_b$, Phase IV) to $(|\uparrow\downarrow\rangle + |\downarrow\uparrow\rangle)/\sqrt{2}$ ($d > d_c$, Phase V), agreeing with the phase boundary given by $U(d_c) = \Delta_f$. It is noted that the higher-order long-range couplings which are ignored in Eq. (3) play little role in the tested parameter region and that other ground states, of center spins $|\downarrow\uparrow\rangle, |\uparrow\downarrow\rangle,$ and $(|\uparrow\downarrow\rangle - |\downarrow\uparrow\rangle)/\sqrt{2}$ are forbidden by the Hamiltonian symmetry. Also, the first excited state changes from $(|\uparrow\downarrow\rangle + |\downarrow\uparrow\rangle)/\sqrt{2}$ to $|\downarrow\downarrow\rangle$ and then to $|\uparrow\uparrow\rangle$ from left to right, in accordance with numerical calculation.

V. NÉEL'S ORDER FORMATION DYNAMICS

Furthermore, we measure the phase formation dynamics during the quantum annealing process. Figure 5 shows the time evolution of Néel's order, defined by $O_N \equiv -\sum_{(i,j) \in E} (\hat{\sigma}^{(i)}(t)\hat{\sigma}^{(j)}(t))/\|E\|$, where $\|E\|$ is the number of edges, along with the up-spin probabilities of individual atoms in G_{10} . With the snap-shot measurements, the adiabatic order formation is clearly observed from the initial paramagnetic phase to the final anti-ferromagnetic phase. The oscillatory behavior is attributed to the finite size. In comparison, a numerical calculation (solid lines) is performed with Lindblad master equations, taking into

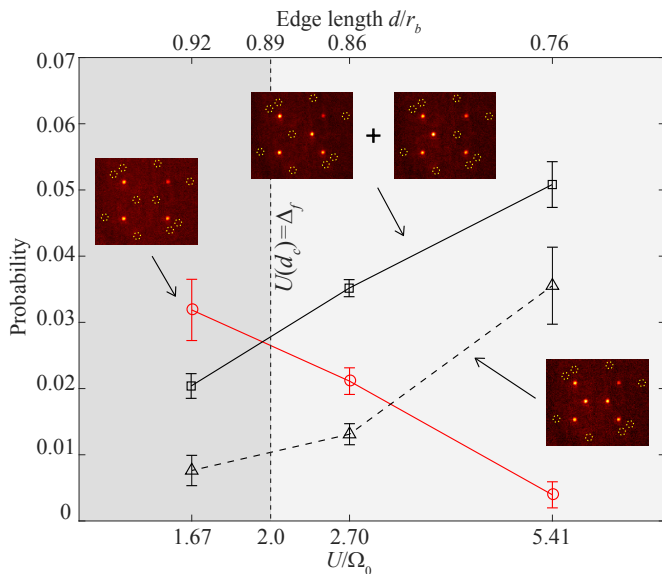


FIG. 4: Probabilities of the low-energy states of Cayley-tree Hamiltonian, $\hat{H}_{G_{14}}(U(d), \Delta_f = 2\Omega_0)$, measured for three different edge lengths, $d/r_b = 0.92, 0.86$, and 0.76 , which correspond to ③, ④, and ⑤, respectively, in the G_{14} phase diagram in Fig. 2(b).

account state-preparation-and-detection (SPAM) errors ($P(|\downarrow\rangle|\uparrow\rangle) = 0.18$, $P(|\uparrow\rangle|\downarrow\rangle) = 0.02$), individual dephasing (~ 36 kHz $\ll \Omega_0$) due to the spontaneous decay during Rydberg excitations, and collective dephasing (~ 3 kHz) from laser phase noise [46]. The numerical calculation in accordance with the observed maximal Néel's order of $O_N(t_f) = 0.48(2)$ indicates that errors are largely due to the SPAM errors accumulated for $N = 10$ atoms. The calculation also suggests that the maximal Néel's order before measurements was $O_N(t_f) = 0.82$ and that the ground-state probability was 61% through the quantum annealing.

VI. EXPERIMENTAL DETAILS

The above experiments were performed with a Rydberg-atom quantum simulator previously reported elsewhere [43, 45–47]. In the quantum simulator, rubidium (^{87}Rb) atoms were initially prepared in the hyperfine ground state, $|\downarrow\rangle = |5S_{1/2}, F = 2, m_F = 2\rangle$, and trapped with optical tweezers. A spatial light modulator (SLM, Meadowlark ODPDM512) was used to create the 3D array of $2N$ optical tweezers and an electrically focus-tunable lens (EL-16-40-TC from Optotune) verified the positions of captured atoms in each atom plane. The SLM was computer-programmed with weighted Gerchberg-Saxton (w-GS) algorithm [48, 49] so that the resulting electric field near each target site (x, y, z) was created as $E(x, y, z) = E_0 \sum_{X, Y} e^{i\Phi(X, Y)} e^{-iT}$, where X, Y are the SLM coordinates on the Fourier plane of

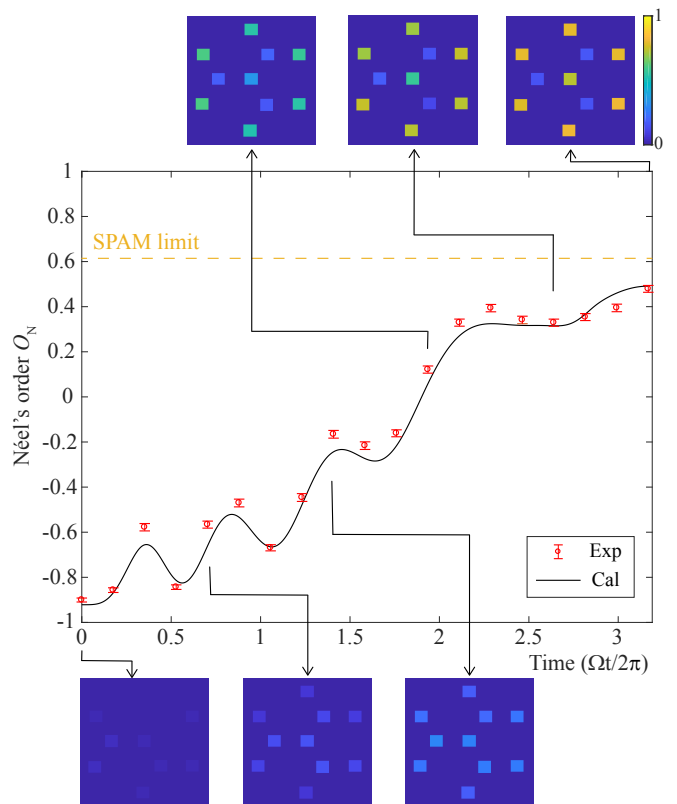


FIG. 5: Quantum annealing dynamics of the Néel's order in the G_{10} Cayley tree are probed as a function of the evolution time and compared with numerical calculations. At chosen times, the Rydberg-state probabilities, $\langle \hat{n} \rangle_j$, of all atoms ($j = 1, \dots, 10$) are shown, being plotted at their respective atom sites.

the optical tweezers, $\Phi(X, Y)$ is the SLM phase pattern, and $T = 2\pi(xX + yY)/f\lambda + \pi z(X^2 + Y^2)/f^2\lambda$ is the transfer kernel. The phase pattern Φ (for $2N$ optical tweezers) was obtained with the w-GS condition, given by $\Phi(X, Y) = \arg(\sum_{j=1}^{2N} w_j E_j(x, y, z) e^{iT_j} / |E_j(x, y, z)|)$, where each weighting factor w_j for j^{th} optical tweezer was optimized through adaptive iterations. The number of the w-GS iterations was about 5, taking about 20 ms time to generate an array of 50 tweezers. Deterministic rearrangement of N atoms to target sites, about $20 \mu\text{m}$ apart from the initial atom reservoir, was performed with consecutive 45 frames of moving traps programmed with phase induction [49]. Over 90% target-occupation probabilities were achieved in 900-ms reconfiguration time and all measurements were performed with defect-free arrangements.

After the atom array was prepared, the optical tweezers were temporarily turned off and the quantum annealing was proceeded. The atoms were excited to the Rydberg state, $|\uparrow\rangle = |71S_{1/2}, m_J = 1/2\rangle$, via the off-resonant intermediate state, $|i\rangle = |5P_{3/2}, F' = 3, m'_F = 3\rangle$. Two lasers (780-nm and 480-nm lasers for $|\downarrow\rangle \rightarrow |i\rangle$ and $|i\rangle \rightarrow$

$|\uparrow\rangle$) were used for the two-photon transition [43]. $\Omega(t)$ and $\Delta(t)$ in $H(t)$ were programmed with a RF synthesizer (Moglabs XRF, 10 MHz) of frequency (780 nm) and amplitude (480 nm) modulations. The modulation ranges were $0 \leq \Omega(t) \leq \Omega_0$ and $-2\Omega_0 \leq \Delta(t) \leq 2\Omega_0$, where the max Rabi frequency was $\Omega_0 = \Omega_{780}\Omega_{480}/(2\Delta') = 1.1 (2\pi)\text{MHz}$ given by $\Omega_{780} = 75 (2\pi)\text{MHz}$, $\Omega_{480} = 19 (2\pi)\text{MHz}$, and $\Delta' = 660 (2\pi)\text{MHz}$ (the intermediate detuning). The van der Waals coefficient [50] was $C_6 = (2\pi)1004 \text{ GHz}\times\mu\text{m}^6$ for $|71S\rangle$ Rydberg-state atoms and the Rydberg blockade radius was $r_b = (C_6/\Omega_0)^{1/6} = 9.8 \mu\text{m}$. The frequency error due to AC Stark shift was small, below 140 kHz, mainly caused by the 480-nm laser. After the quantum annealing, the optical tweezers were turned back on and the atom states in the ground state ($|\downarrow\rangle$) were measured whether they survived ($|\downarrow\rangle$) or not ($|\uparrow\rangle$). Each measurement in Fig. 3 was repeated by 672, 2208, and 5113 times respectively for G_{10} , G_{22} , and G_{14} to obtain the accumulated probability distributions.

VII. CONCLUSION

We have explored the possibilities of Rydberg-atom quantum simulators towards high-dimensional qubit connec-

tion programming. With up to $N = 22$ rubidium single atoms arranged in three-dimensional space, we have programmed Ising Hamiltonians on three different Cayley tree graphs. The anti-ferromagnetic phase in regular Cayley trees and frustrated competing ground-states in a dual-center Cayley tree are directly observed, showing good agreement with model calculations. There are many hopes to utilize the potentials of Rydberg-atom quantum simulators in large-scale implementations and high-dimensional configurability [25–27, 51–53]. It is hoped that 3D-qubit configurations of Rydberg-atom quantum annealers shall be useful for efficient and programmable quantum optimization problems.

Acknowledgments

This research was supported by Samsung Science and Technology Foundation (SSTF-BA1301-52), National Research Foundation of Korea (NRF) (2017R1E1A1A01074307), and Institute for Information & Communications Technology Promotion (IITP-2018-2018-0-01402).

-
- [1] E. Farhi, J. Goldstone, S. Gutmann, J. Lapan, A. Lundgren, and D. Preda, “A Quantum adiabatic evolution algorithm applied to random instances of an NP-complete problem,” *Science* **292**, 472 (2001).
- [2] A. Das and B. K. Chakrabarti, “*Colloquium*: Quantum annealing and analog quantum computation,” *Rev. Mod. Phys.* **80**, 1061 (2008).
- [3] T. Albash and D. A. Lidar, “Adiabatic quantum computation,” *Rev. Mod. Phys.* **90**, 015002 (2018).
- [4] P. Hauke, H. G. Katzgraber, W. Lechner, H. Nishimori, and W. D. Oliver, “Perspectives of quantum annealing: methods and implementations,” *Rep. Prog. Phys.* **83**, 054401 (2020).
- [5] M. W. Johnson *et al.*, “Quantum annealing with manufactured spins,” *Nature* **473**, 194 (2011).
- [6] P. I. Bunyk *et al.*, “Architectural Considerations in the Design of a Superconducting Quantum Annealing Processor,” *IEEE Trans. Appl. Supercond.* **24**, 1 (2014).
- [7] D. Rosenberg *et al.*, “3D integrated superconducting qubits,” *Npj Quantum Inf.* **3**, 42 (2017).
- [8] M. P. Harrigan, K. J. Sung, M. Neeley, *et al.*, “Quantum approximate optimization of non-planar graph problems on a planar superconducting processor,” *Nat. Phys.* (2021). <https://doi.org/10.1038/s41567-020-01105-y>
- [9] S. Korenblit *et al.*, “Quantum simulation of spin models on an arbitrary lattice with trapped ions,” *New J. Phys.* **14**, 095024 (2012).
- [10] R. Islam *et al.*, “Emergence and frustration of magnetism with variable-range interactions in a quantum simulator,” *Science* **340**, 583 (2013).
- [11] P. Richerme, C. Senko, J. Smith, A. Lee, S. Korenblit, and C. Monroe, “Experimental performance of a quantum simulator: Optimizing adiabatic evolution and identifying many-body ground states,” *Phys. Rev. A* **88**, 012334 (2013).
- [12] P. Hauke, L. Bonnes, M. Heyl, and W. Lechner, “Probing entanglement in adiabatic quantum optimization with trapped ions,” *Front. Phys.* **3**, 21 (2015).
- [13] R. Babbush, P. J. Love, and A. Aspuru-Guzik, “Adiabatic quantum simulation of quantum chemistry,” *Sci. Rep.* **4**, 6603 (2014).
- [14] H. Neven, V. S. Denchev, G. Rose, and W. G. Macready, “Training a binary classifier with the quantum adiabatic algorithm,” *arXiv:0811.0416*
- [15] E. G. Rieffel, D. Venturelli, B. O’Gorman, M. B. Do, E. M. Prystay, and V. N. Smelyanskiy, “A case study in programming a quantum annealer for hard operational planning problems,” *Quant. Inf. Proc.* **14**, 1 (2015).
- [16] K. C. Young, M. Sarovar, and R. Blume-Kohout, “Error suppression and error correction in adiabatic quantum computation: techniques and challenges,” *Phys. Rev. X* **3**, 041013 (2013).
- [17] S. Boixo, T. F. Rønnow, S. V. Isakov, Z. Wang, D. Wecker, D. A. Lidar, J. M. Martinis, and M. Troyer, “Evidence for quantum annealing with more than one hundred qubits,” *Nat. Phys.* **10**, 218 (2014).
- [18] K. L. Pudenz, T. Albash, and D. A. Lidar, “Error-corrected quantum annealing with hundreds of qubits,” *Nat. Commun.* **5**, 3243 (2014).
- [19] S. Ebadi, T. T. Wang, H. Levine, A. Keesling, G. Semeghini, A. Omran, D. Bluvstein, R. Samajdar, H. Pichler, W. W. Ho, S. Choi, S. Sachdev, M. Greiner, V. Vuletić, and M. D. Lukin, “Quantum phases of matter on a 256-atom programmable quantum simulator,”

- arXiv:2012.12281
- [20] P. Scholl, M. Schuler, H. J. Williams, A. A. Eberharter, D. Barredo, K.-N. Schymik, V. Lienhard, L.-P. Henry, T. C. Lang, T. Lahaye, A. M. Läuchli, and A. Browaeys, “Programmable quantum simulation of 2D antiferromagnets with hundreds of Rydberg atoms,” arXiv:2012.12268
- [21] B. Altshuler, H. Krovi, and J. Roland, “Anderson localization makes adiabatic quantum optimization fail,” *Proc. Natl. Acad. Sci.* **107**, 12446 (2010).
- [22] R. D. Somma, D. Nagaj, and M. Kieferová, “Quantum speedup by quantum annealing,” *Phys. Rev. Lett.* **109**, 050501 (2012).
- [23] T. F. Rønnow, Z. Wang, J. Job, S. Boixo, S. V. Isakov, D. Wecker, J. M. Martinis, D. A. Lidar, and M. Troyer, “Defining and detecting quantum speedup,” *Science* **345**, 420 (2014).
- [24] S. Muthukrishnan, T. Albash, and D. A. Lidar, “Sensitivity of quantum speedup by quantum annealing to a noisy oracle,” *Phys. Rev. A* **99**, 032324 (2019).
- [25] W. Lechner, P. Hauke, and P. Zoller, “A quantum annealing architecture with all-to-all connectivity from local interactions,” *Sci. Adv.* **1**, e1500838 (2015).
- [26] A. W. Glaetzle, R. M. van Bijnen, P. Zoller and W. Lechner, “A coherent quantum annealer with Rydberg atoms,” *Nat. Commun.* **8**, 15813 (2017).
- [27] H. Pichler, S.-T. Wang, L. Zhou, S. Choi, and M. D. Lukin, “Quantum Optimization for Maximum Independent Set Using Rydberg Atom Arrays,” arXiv:1808.10816
- [28] H. Weimer, M. Müller, I. Lesanovsky, P. Zoller, and H. P. Büchler, “A Rydberg quantum simulator,” *Nat. Phys.* **6**, 382 (2010).
- [29] A. Browaeys and T. Lahaye, “Many-body physics with individually controlled Rydberg atoms,” *Nat. Phys.* **16**, 132 (2020).
- [30] W. Lee, H. Kim, and J. Ahn, “Three-dimensional rearrangement of single atoms using actively controlled optical microtraps,” *Opt. Express* **24**, 9816 (2016).
- [31] H. Kim, W. Lee, H.-g. Lee, H. Jo, Y. Song, and J. Ahn, “In situ single-atom array synthesis by dynamic holographic optical tweezers,” *Nat. Commun.* **7**, 13317 (2016).
- [32] D. Barredo, S. de Léséleuc, V. Lienhard, T. Lahaye, and A. Browaeys, “An atom-by-atom assembler of defect-free arbitrary 2d atomic arrays,” *Science* **354**, 1021 (2016).
- [33] M. Endres, H. Bernien, A. Keesling, H. Levine, E. R. Anschuetz, A. Krajenbrink, and M. D. Lukin, “Atom-by-atom assembly of defect-free one-dimensional cold atom arrays,” *Science* **354**, 1024 (2016).
- [34] D. Barredo, V. Lienhard, S. de Léséleuc, T. Lahaye, and A. Browaeys, “Synthetic three-dimensional atomic structures assembled atom by atom,” *Nature* **561**, 79 (2018).
- [35] T. Pohl, E. Demler, and M. D. Lukin, “Dynamical crystallization in the dipole blockade of ultracold atoms,” *Phys. Rev. Lett.* **104**, 043002 (2010).
- [36] P. Schauss, J. Zeiher, T. Fukuhara, S. Hild, M. Cheneau, T. Macri, T. Pohl, I. Bloch, and C. Gross, “Crystallization in Ising quantum magnets,” *Science* **347**, 1456 (2015).
- [37] H. Bernien, S. Schwartz, A. Keesling, H. Levine, A. Omran, H. Pichler, S. Choi, A. S. Zibrov, M. Endres, M. Greiner, V. Vuletić, and M. D. Lukin, “Probing many-body dynamics on a 51-atom quantum simulator,” *Nature* **551**, 579 (2017).
- [38] V. Lienhard, S. de Léséleuc, D. Barredo, T. Lahaye, and A. Browaeys, M. Schuler, L.-P. Henry, and A. M. Läuchli, “Observing the space- and time-dependent growth of correlations in dynamically tuned synthetic Ising models with antiferromagnetic interactions,” *Phys. Rev. X* **8**, 021070 (2018).
- [39] I. I. Beterov, D. B. Tretyakov, V. M. Entin, E. A. Yakshina, I. I. Ryabtsev, M. Saffman, and S. Bergamini, “Application of adiabatic passage in Rydberg atomic ensembles for quantum information processing,” *J. Phys. B: At. Mol. Opt. Phys.* **53**, 182001 (2020).
- [40] H. A. Bethe, “Statistical theory of superlattices,” *Proc. Roy. Soc. A* **150**, 552 (1935).
- [41] M. Ostilli, “Cayley trees and Bethe lattices: a concise analysis for mathematicians and physicists,” *Physica A* **391**, 3417 (2011).
- [42] R. J. Baxter, *Exactly Solvable Models in Statistical Mechanics* (Academic Press, 1982).
- [43] M. Kim, Y. Song, J. Kim, and J. Ahn, “Quantum-Ising Hamiltonian programming in trio, quartet, and sextet qubit systems,” *PRX Quantum* **1**, 020323 (2020).
- [44] A. Lucas, “Ising formulations of many NP problems,” *Front. Phys.* **2**, 5 (2014).
- [45] H. Kim, Y. J. Park, K. Kim, H.-S. Sim, and J. Ahn, “Detailed balance of thermalization dynamics in Rydberg atom quantum simulators,” *Phys. Rev. Lett.* **120**, 180502 (2018).
- [46] W. Lee, M. Kim, H. Jo, Y. Song, and J. Ahn, “Coherent and dissipative dynamics of entangled few-body systems of Rydberg atoms,” *Phys. Rev. A* **99**, 043404 (2019).
- [47] H. Jo, Y. Song, M. Kim, and J. Ahn, “Rydberg Atom Entanglements in the Weak Coupling Regime,” *Phys. Rev. Lett.* **124**, 033603 (2020).
- [48] R. Di Leonardo, F. Ianni, and G. Ruocco, “Computer generation of optimal holograms for optical trap arrays,” *Opt. Express* **15**, 1913 (2007).
- [49] H. Kim, M. Kim, W. Lee, and J. Ahn, “Gerchberg-Saxton algorithm for tweezer-trap atom arrangements,” *Opt. Express* **27**, 2184 (2019).
- [50] S. Weber, C. Tresp, H. Menke, A. Urvoy, O. Firstenberg, H. P. Büchler, and S. Hofferberth, “Tutorial: Calculation of Rydberg interaction potentials,” *J. Phys. B: At. Mol. Opt. Phys.* **50**, 133001 (2017).
- [51] S. Diehl, E. Rico, M. A. Baranov, and P. Zoller, “Topology by dissipation in atomic quantum wires,” *Nature Physics* **7**, 971 (2011).
- [52] M. F. Serret, B. Marchand, and T. Ayrál, “Solving optimization problems with Rydberg analog quantum computers: Realistic requirements for quantum advantage using noisy simulation and classical benchmarks,” arXiv:2006.11190
- [53] X. Qiu, P. Zoller, and X. Li, “Programmable quantum annealing architectures with Ising quantum wires,” arXiv:2008.00006